Journal of Power Sources 196 (2011) 6425–6432

Contents lists available at ScienceDirect

Journal of Power Sources

journal homepage: www.elsevier.com/locate/jpowsour

Nanostructured Fe_2O_3 and CuO composite electrodes for Li ion batteries synthesized and deposited in one step

E. García-Tamayo*, M. Valvo, U. Lafont, C. Locati, D. Munao, E.M. Kelder

NanoStructuredMaterials, Department of Chemical Engineering, TUDelft, 2628 BL Delft, The Netherlands

ARTICLE INFO

Article history:
Received 19 November 2010
Received in revised form 24 February 2011
Accepted 27 March 2011
Available online 8 April 2011

Keywords:
Electrospray pyrolysis
Li ion batteries
Conversion reaction
One step synthesis

ABSTRACT

Nanostructured composite electrodes based on iron and copper oxides for applications in Li-ion batteries are produced by Electrostatic spray pyrolysis (ESP). The electrodes are directly formed by electrospraying precursor solutions containing either iron or copper salts dissolved in N-methylpyrrolidone (NMP) together with polyvinylidene fluoride (PVdF) as binder. The morphology and the structure of the deposited electrodes are investigated by X-ray diffraction (XRD) and Transmission electron microscopy (TEM), which show that sub-micrometric deposits are formed as a composite of oxide nanoparticles of a few nanometers in a PVdF polymer matrix. Electrochemical characterization by cyclic voltammetry (CV) and galvanostatic charge–discharge tests demonstrate that the conversion reactions in these electrodes enable initial discharge capacities of about 800 mAh g^{-1} and 1550 mAh g^{-1} for CuO and Fe_2O_3, respectively. The capacity retention in both cases needs further improvements.

1. Introduction

Li-ion batteries are one of the most popular power sources that are currently used to power up a wide range of portable electronic devices. However, the portability of these devices implies that they become increasingly thinner, smaller and lighter, therefore requiring batteries with enhanced energy and power densities. Furthermore, high-power applications (e.g., EVs, HEVs, power tools) require even higher volumetric and gravimetric energy densities, which can be eventually achieved by employing new materials in order to improve the existing Li-ion battery technology. Intercalation represents the reaction mechanism on which rechargeable Li-ion batteries have always relied since their first commercial release by Sony [1]. Intercalation reactions in negative electrodes and their characteristic properties have been widely discussed and reviewed [2,3]. The major drawback of this mechanism is related to its limited capacities. In the case of graphite, it is possible to reversibly store only one atom of lithium per 6 atoms of carbon (i.e., LiC_6), corresponding to a theoretical capacity of about 370 mAh g^{-1}. It has been shown that lithium can react with a range of transition metal–oxides (TMO) by a process referred to as conversion [4]. The main advantage of TMO over carbonaceous materials in negative electrodes is that their capacities are noticeably higher (i.e., up to 1000 mAh g^{-1}), due to their ability to incorporate more than one Li atom per MO. Previous works adopting this approach have been reported [5–9], pointing out the crucial role that nanostructured materials can play in these systems, as well as in other energy conversion and storage applications [10–14]. Copper and iron oxides nanoparticles are of particular interest because they can be produced using low-cost precursors with a limited impact on the environment. However, negative electrodes based on these materials suffer from mechanical volume changes during Li uptake and removal, conferring an important role to the processes of particle synthesis as well as electrode assembly, where the active particles are mixed with other inactive components (i.e., binders and additives). In this study, Fe_2O_3 and CuO nanostructured electrodes are synthesized in one step via Electrostatic spray pyrolysis (ESP). During the processing the oxide nanoparticles are generated and thereby mixed immediately with the binder (i.e., PVdF) so as to form the composite electrodes and hence avoiding powder mixing and paste casting. It is important to note that ESP has been conveniently applied to the synthesis and deposition of various functional coatings like MgO [15], ZrO_2 [16], as well as thin film electrodes for Li-ion batteries. Different materials have been synthesized in that respect, e.g., $Li_{1.2}Mn_2O_4$ [17], $LiMn_2O_4$ [18], $LiCoO_2$ [19,20], $Li_4Ti_5O_{12}$ [21] for positive electrodes and Fe_2O_3 [22], SnO_2 [23] for negative electrodes. However, all these materials do not include any polymer for binding purposes. The presence of the binder promotes the mutual adhesion of the deposits, as well as their overall contact with the underlying substrate to obtain a reinforced composite electrode coating. This circumstance should be also addressed when internal and external mechanical stresses are present. A similar approach using a precursor ink consisting of a solution of polymer binder with a suspension of previously

* Corresponding author. Tel.: +31 68365 4464; fax: +31 15278 5536.
E-mail address: e.garciatamayo@tudelft.nl (E. García-Tamayo).

0378-7753/$ – see front matter © 2011 Elsevier B.V. All rights reserved.
doi:10.1016/j.jpowsour.2011.03.066

synthesized silicon nanoparticles and commercial carbon additive has been recently reported [24]. Here Fe_2O_3 and CuO nanoparticles of few nanometers have been directly generated, dispersed and coated together with PVdF in composite negative electrodes without the need of any further processing.

2. Materials and methods

A schematic of the equipment used for the production of the Fe_2O_3 and CuO nanostructured composite electrodes is shown in Fig. 1(a). It consists mainly of three sections, namely: (1) a high voltage power supply connected to a nozzle and a heated substrate holder (grounded) that is attached to a temperature controller; (2) a pumping unit, where a precursor solution can be injected in a controlled manner via a syringe pump; (3) a reaction chamber, where the sample is placed and the atomization of the liquid precursors occurs followed by pyrolysis reactions.

The precursor solutions were prepared from iron (II) acetate anhydrous, $Fe(C_2H_3O_2)_2$ (Alfa® GmbH) and copper (II) nitrate trihydrate, $Cu(NO_3)_2{\cdot}3H_2O$ (AnalaR® BDH). These salts were independently mixed with polyvinylidene fluoride (PVdF SOLEF 1015) in a weight ratio (Metal:PVdF wt%) of 5:1 and were, respectively dissolved in 15 ml of N-methyl-2-pyrrolidone (NMP MERCK-Schuchardt). Vigorous stirring was applied in order to achieve a complete dissolution of the PVdF and the precursor salts. No carbon black was added to the precursor solutions for the experiments. The solutions were fed to the electrified nozzle at a constant flow rate in order to undergo electrospraying and direct reaction so as to deposit electrodes on coin cell cans. The high electrical field applied between the nozzle and the substrate holder caused the formation and acceleration of tiny, highly charged droplets towards the substrate. The atomization process was accompanied by the evaporation of the solvent and subsequent pyrolysis of the precursor salts, enabling the direct formation of coated nanocomposite electrodes without any 'doctor-blading' method [25,26]. The distance between the tip of the nozzle and the support was kept constant at 20 mm during the electrode deposition, as well as the injection flow rate (values are reported in Table 1). The applied voltage was tuned in each experiment in order to reach a stable electrospray in the so-called cone-jet mode, which was observed by means of a high intensity lamp. The temperature of the substrate was kept constant at 280 °C to ensure complete evaporation of the solvent (i.e., NMP evaporates around 200 °C) and to obtain pyrolysis of the precursors, as well as good adhesion of the PVdF to the coin cell can substrates. Adjusting the physical parameters of the ESP allows control of the morphology, thickness and texture (i.e., porosity) of the deposited layers. The electrode thickness can be controlled, for example, by adjusting the deposition time on the substrate. The morphology and texture can be influenced by adjusting flow rate, voltage, distance from nozzle to sample, as well as by taking into account properties of the solvent, like its temperature of evaporation, viscosity, conductivity, etc. A mask was used to control the area of deposition on the coin cell cans in order to obtain circular coatings of approximately 150 mm^2. It is worth mentioning that the resulting electrodes do not need any further treatment and that they can be directly sealed in a full battery assembly by adding the remaining parts (i.e., electrolyte-soaked separator, lithium disk, spring, gasket and stainless steel lid).

The deposited mass and thickness of the PVdF–oxide composites were determined by carrying out measurements on the coin cell cans before and after the process of electrode coating. For this purpose a digital balance (Sartorius) with an accuracy of 10^{-2} mg and a digital caliper (Mitutoyo Absolute, 10^{-3} mm accuracy) were employed. The measured values of thickness and mass obtained in correspondence of different sprayed volumes for the precursors are shown in Fig. 2. As it can be seen, increasing the thickness of the coating results in a growth of the mass deposited on the coin cell cans.

The mass percentage of the oxide materials in the composite electrodes was then calculated by means of the weight ratio of the PVdF/precursor salts and their respective pyrolysis reactions, yielding approximately 69% for Fe_2O_3 and 62% for CuO. Galvanostatic measurements were performed in order to assess the electrochemical performance of the coated electrodes on CR2320-type coin cells assembled in a He-filled glove box ($H_2O < 2$ ppm). The nanostructured coatings were directly tested as working electrodes, while lithium metal disks were used as reference and counter electrodes with polyethylene separators (Solupor) soaked with an electrolyte solution of 1 M $LiPF_6$ in EC:DMC 2:1 (Mitsubishi Chemical). The cells were discharged and charged on a Maccor S-4000 cycler between 3.0 V and 0.05 V at gravimetric current densities of 124 mAg^{-1} for Fe_2O_3/PVdF and 337 mAg^{-1} for CuO/PVdF, respectively. Atomic force microscopy (AFM) was performed on the coated samples by a NT-MDT NTEGRA scanning probe microscope in semi-contact mode by a Si cantilever and tip. A Philips CM30T transmission electron microscope operated at 300 kV was used to investigate the morphology, size and crystallinity of the as-deposited nanocomposites. An EDX probe (Oxford) coupled to the TEM was further used to perform an elemental analysis of the materials. Their composition and crystalline structure were also studied by means of X-ray diffraction (Bruker AXS D8 Advance, Cu-K_α).

3. Results and discussion

3.1. Structural and morphological characterization

The morphology of the coated materials was investigated by AFM. The images of the scanned areas for the composite CuO/PVdF and Fe_2O_3/PVdF electrodes are shown in Fig. 3(a and b), respectively.

Fig. 3(a) shows that sub-micrometric deposits of CuO/PVdF have been formed. The observed elongated features are composed of smaller spherical-like structures merged together in agglomerates arranged in platelets. The surface morphology suggests that the pore size is similar to that of the particles. In Fig. 3(b) the surface of the Fe_2O_3/PVdF coating displays similar characteristics, showing, however, larger and more defined spherical deposits arranged in three dimensional agglomerates. The resulting pore size is comparable with that of the agglomerates.

XRD was performed on samples synthesized under identical conditions to those described for the preparation of each oxide/PVdF electrode, but having a larger area coverage and a thicker coating. The underlying substrates were either aluminum or stainless steel.

In Fig. 4(a), the diffraction pattern of the CuO/PVdF composite is presented. The sharpest peaks at 45°, 65° and 78°, correspond to characteristic diffractions related to the underlying Al foil support. The observed pattern indicates that monoclinic CuO (JCPDS: 80-1916) has been formed, as also confirmed by the black color of the coated material. Two broad peaks around 35° and 38° correspond to the strongest characteristic diffractions by the planes (−1 1 0) and (1 1 1), respectively. Four weak features can be also observed in the diffraction pattern around 33° (110), 49° (−202), 58° (202) and 62° (−113), respectively, confirming the presence of small crystallites of CuO. Moreover, the average crystallite size was evaluated by the Scherrer formula which yielded an approximate value of 12 nm for this material. Fig. 4(b) shows the diffraction pattern of the Fe_2O_3/PVdF layer. The only peaks that are clearly visible in the plot are those related to the stainless steel substrate, while the

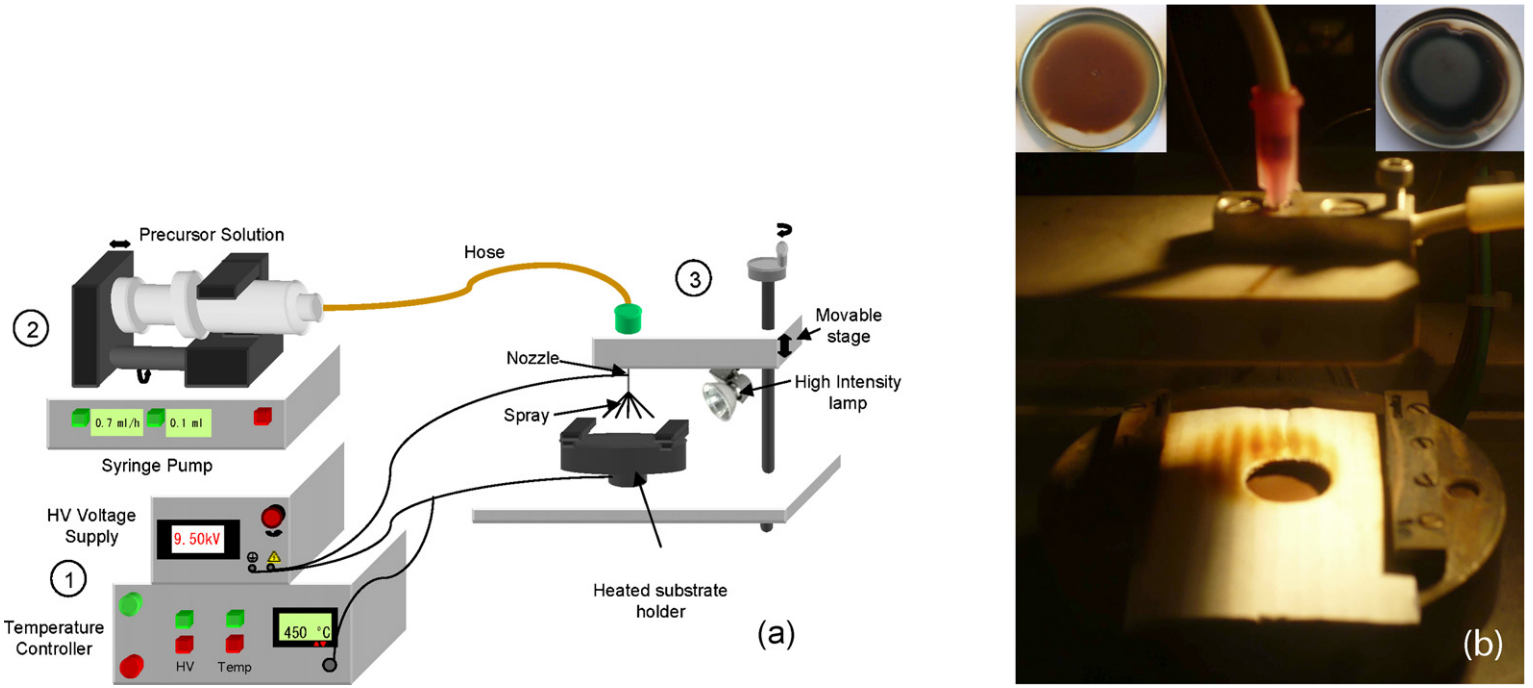

Fig. 1. Schematic drawing (a) and photo (b) of the electrostatic spray deposition setup used for the direct synthesis and assembly of coated nanocomposite electrodes. The insets in (b) show examples of composite coatings with PVdF. Top left-hand corner: Fe_2O_3, top right-hand corner: CuO.

Table 1
Experimental parameters and characteristics of the reacted materials.

Precursor	Voltage (kV)	Current (mA)	Flow rate (mLh^{-1})	Nozzle (mm)	Temperature (°C)	Expected material	Estimated % of active material
$Cu(NO_3)_2$ + NMP + PVdF	~8.4	~0.002	0.2	20	280	CuO + PVdF	62
$Fe(Ac)_2$ + NMP + PVdF	~8.0	~0.001	0.4	20	280	Fe_2O_3 + PVdF	69

ESP parameters and characteristics of the obtained electrodes.

nanocomposite layer displays mainly amorphous characteristics. Nevertheless, the broad hump around 33° falls within the angular range where the strongest diffractions of Fe_2O_3 occur. Indeed, characteristic diffractions by the planes (1 0 4) and (1 1 0) for α-Fe_2O_3 are, respectively due at 33.15 and 35.61° (JCPDS no. 33-0664). Furthermore, γ-Fe_2O_3 displays its strongest peak indexed (3 1 1) at 35.65° (JCPDS no. 39-1346). The reduced size of the nanoparticles and the relatively low temperature for the synthesis process are likely responsible for the observed diffraction pattern. Nevertheless, the dark reddish-brown color of the coatings clearly indicates that Fe_2O_3 has been formed, since other iron oxides with different stoichiometries have a distinctive black color.

Investigation of the morphology and the intimate structure of the materials was performed by TEM. Fig. 5(a) is a bright field image that shows the structure of the composite CuO/PVdF deposits. Small CuO nanoparticles with sizes of roughly 4–7 nm are observed. The CuO nanoparticles, which correspond to the dark dots in the image, are homogeneously interdispersed in the PVdF. The high resolution TEM image in Fig. 5(b) shows the crystalline nature of the nanosized particles. Lattice fringes are clearly seen in the dotted circles that serve as a guide for the eyes. The data agree well with the calculated crystallite size derived from XRD. It can be further concluded that the nanoparticles are mainly nanocrystals.

Fig. 6(a) shows the morphology of the nanocomposite Fe_2O_3/PVdF. The spherical shape of the deposits is caused by the drying process of the electrosprayed precursor droplets. Also in this case a fine interdispersion of the oxide particles in PVdF is achieved. Fig. 6(b) presents a highly magnified image of one of these spherical-like relics, showing that Fe_2O_3 particles of about 5–7 nm are homogeneously distributed in these structures. Moreover, no lattices fringes are observed in this material, confirming the amorphous-like nature of the iron oxide, as previously shown by the XRD analysis.

The local chemical composition of these oxide particles was further investigated by energy dispersive X-rays analysis, yielding about 40% of iron and 60% of oxygen, matching with the Fe_2O_3 stoichiometry.

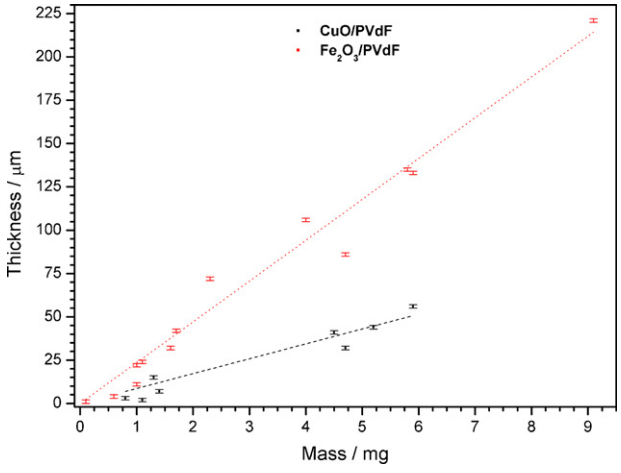

Fig. 2. Plot of the values of thickness *vs.* mass for the deposited electrodes of Cu/PVdF (open stars) and Fe_2O_3/PVdF (solid stars) obtained for various sprayed volumes of the precursor solutions.

3.2. Electrochemical performances of the electrode materials

The electrochemical behaviour of the coated electrodes was investigated by cyclic voltammetry (CV) and galvanostatic tests. Fig. 7 shows the CV plot of the CuO/PVdF electrode which was scanned at a rate of 0.1 mVs^{-1}. During the first cycle, three cathodic peaks are observed at 2.4, 1.25 and 0.7 V. These peaks can be associated, respectively to a multistep reaction related to the creation of a $Cu^{II}_{1-x}Cu^{I}_{x}O_{1-x/2}(0 \le x \le 0.4)$ solid solution within a CuO phase, the formation of a Cu_2O phase and finally the decomposition into metallic Cu and Li_2O [27,28]. Besides, at high lithiation stages (i.e., between 0.02 and 0.3 V), another reduction process is present, which can be attributed to the reduction of the electrolyte solvent and hence the growth of an organic-type layer. Conversely, two anodic peaks appear at 2.5 V and 2.75 V, which are, respectively due to the oxidation of metallic Cu–Cu(I) and to the partial oxidation of Cu(I)–Cu(II). The broad bump around 1.45 V could be associated to decomposition of the organic layer [27,28]. The CV peaks and their variations are consistent with the galvanostatic discharge–charge plots shown in Fig. 8(a). Three distinct potential slopes are visible in both the first discharge and charge curves, which are observed more clearly as peaks in the related differential capacity *vs.* voltage

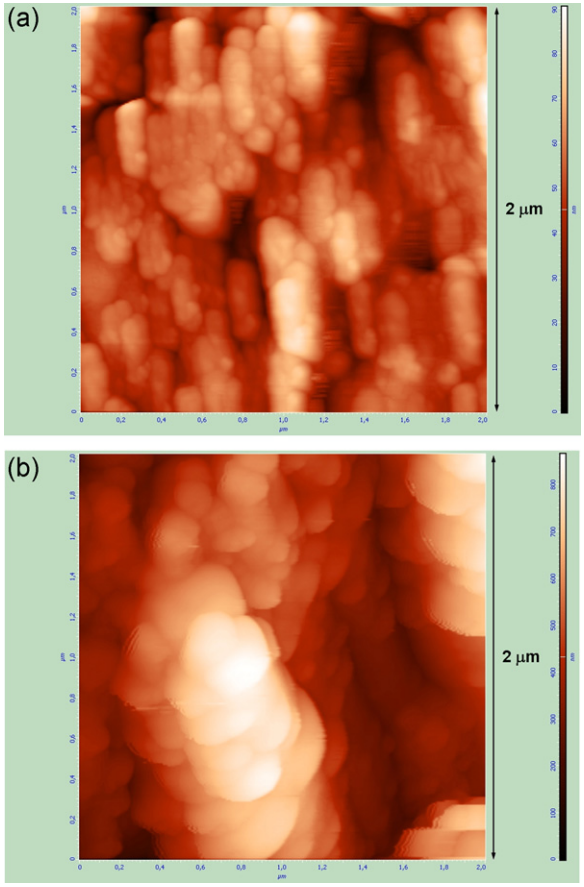

Fig. 3. AFM images of the surface morphology of the nanocomposites. (a) Scan of CuO/PVdF and (b) Fe_2O_3/PVdF. The scanned areas are 2 µm × 2 µm wide.

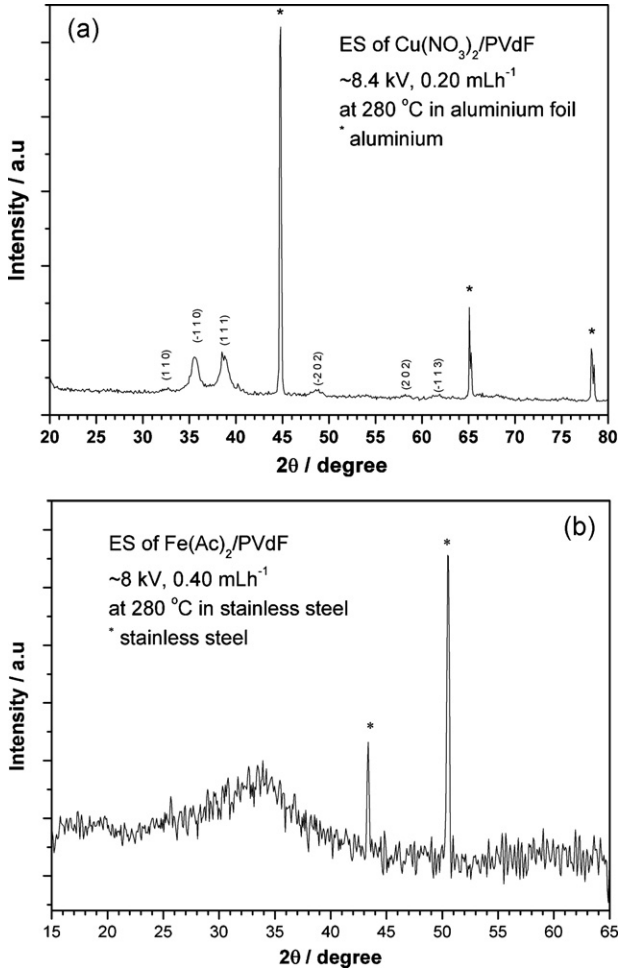

Fig. 4. XRD spectra of the nanocomposite electrodes by electrostatic spray pyrolysis of (a) $Cu(NO_3)_2{\cdot}3H_2O$/PVdF and (b) $Fe(C_2H_3O_2)_2$/PVdF at 280 °C. The peaks marked by an asterisk refer to the characteristic diffractions of the substrates used.

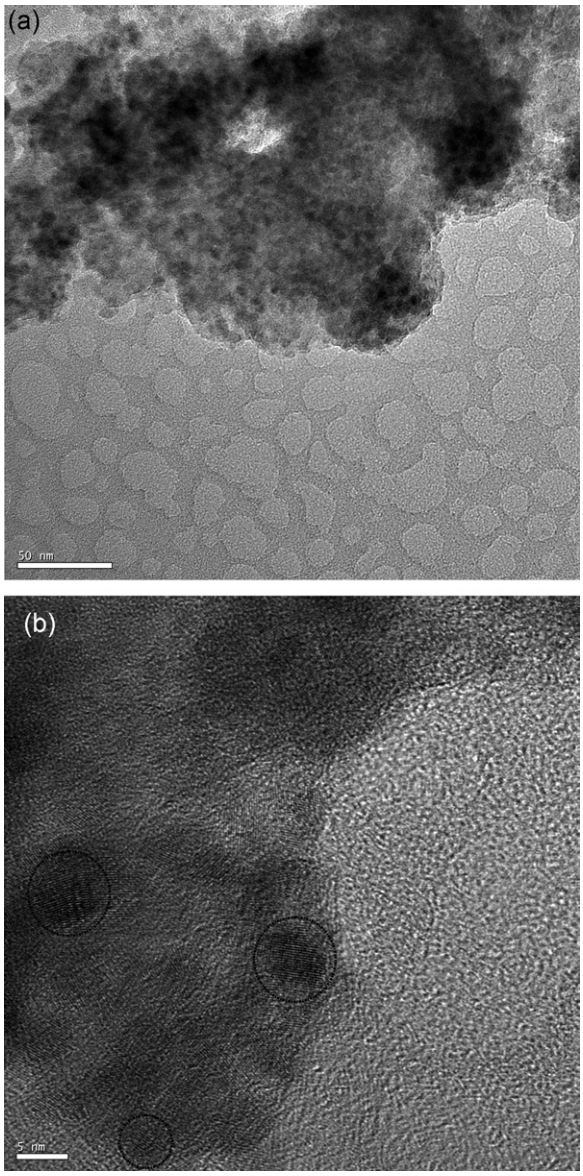

Fig. 5. TEM bright field images showing (a) morphology and size of the CuO/PVdF nanocomposites and (b) lattice fringes of CuO at high resolution.

plot (see figure inset). Following the direction of the arrow in the plot three different peaks are noticed at 2.4 V (wide bump), 1.3 V and 0.8 V, respectively. Similarly, a broad peak around 1.45 V followed by two other peaks at 2.35 and 2.7 V are observed in the upper curve corresponding to the charge process. It is important to observe that for this material a remarkable difference in the charge–discharge processes exists in terms of characteristic voltages at which the reactions take place. In this respect, it is necessary to charge the system above 2.0 V in order to extract most of the Li that has been stored during a former discharge. The CuO/PVdF electrode displayed a discharge capacity of about 800 mAh g^{-1} in the first cycle at a gravimetric current density of 337 mAg^{-1}. It is interesting to note that after the first cycle the subsequent discharge curves show a more pronounced step-like profile, with a typical upper shift of the voltage plateau around 1.3–1.4 V due to the enhanced tendency of dissolution of the regenerated nano CuO after initial reaction with Li, discovered for the CuO/Li primary battery [29].

Fig. 8(b) presents the evolution of charge and discharge capacities upon cycling. A clear capacity fading is observed in the first cycle, however, it should be noted that the CuO/PVdF electrode is able to cycle at a relatively high gravimetric current density, without the presence of any carbon additive and a non-negligible fraction of PVdF, which hinders electron conduction. The small CuO nanoparticles and their homogenous dispersion in the coating play a key role in the performance of the electrode, which shows a capacity of about 360 mAh g^{-1} after 25 cycles.

The electrochemical behaviour of Fe_2O_3/PVdF electrode was investigated in a similar way. Fig. 9 shows the CV plot for the first three cycles at a rate of 0.1 mVs^{-1}. In the first scan a cathodic peak around 0.67 V can be observed, which could be associated to the initial formation of the SEI layer and the conversion reaction of Fe_2O_3 into Fe^0 and Li_2O [30]. In the following anodic part a clear oxidation peak is observed at about 1.50 V, accompanied by a broad shoulder around 1.75 V. During subsequent cycles these features do not shift but they gradually merge. These two features can be associated to the decomposition of the SEI layer and the reversible oxidation of Fe^0–Fe^{3+} [31,32]. In the subsequent cycles the cathodic and anodic peaks slightly shift to 0.70 V and 1.55 V, respectively. Furthermore, the intensity of the peaks, as well as their respective subtended areas decrease upon cycling indicating loss of capacity. The origin of the small reduction peak that appears around 1.30 V is unclear but it could be related to the reaction of the electrolyte with the nanoparticles left after the first cycle of conversion and regeneration.

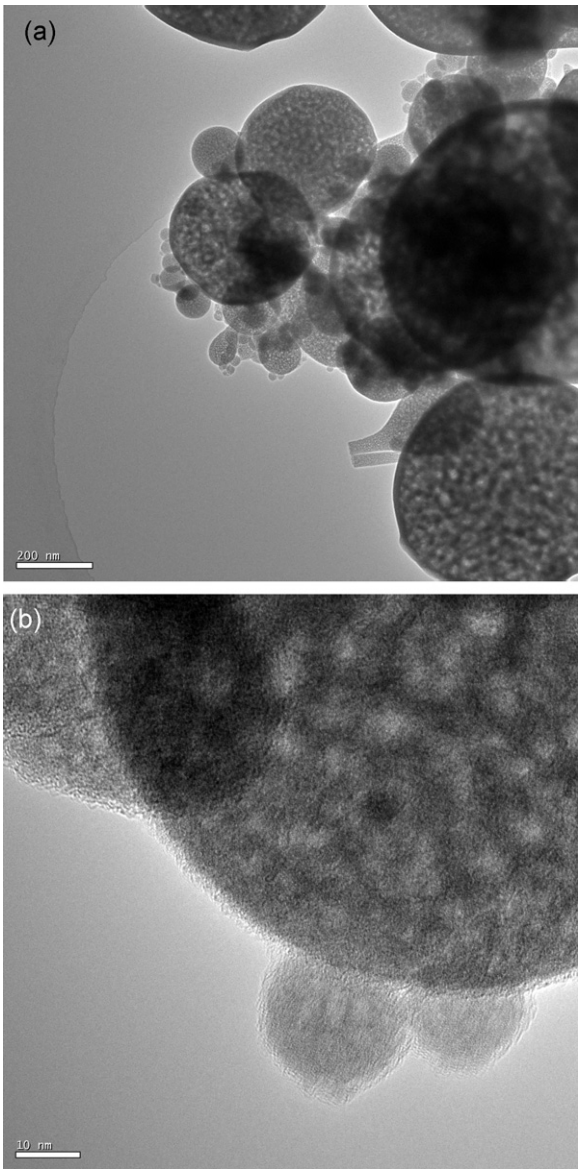

Fig. 6. TEM bright field images showing (a) morphology and size of the Fe_2O_3/PVdF nanocomposites and (b) local structure at high resolution showing the absence of lattice fringes.

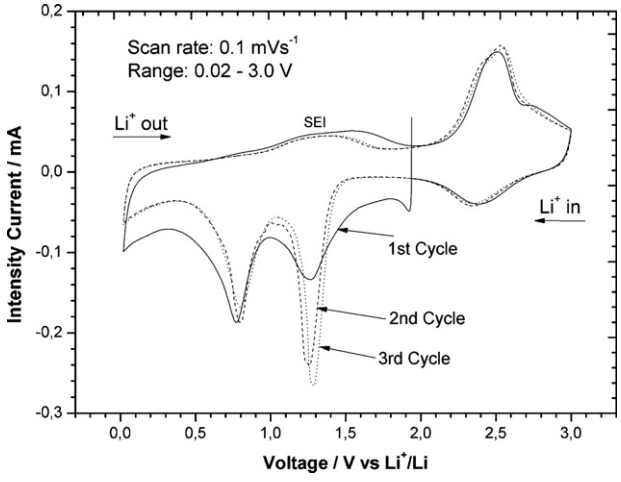

Fig. 7. CV plot for the CuO/PVdF electrode deposited by ESP.

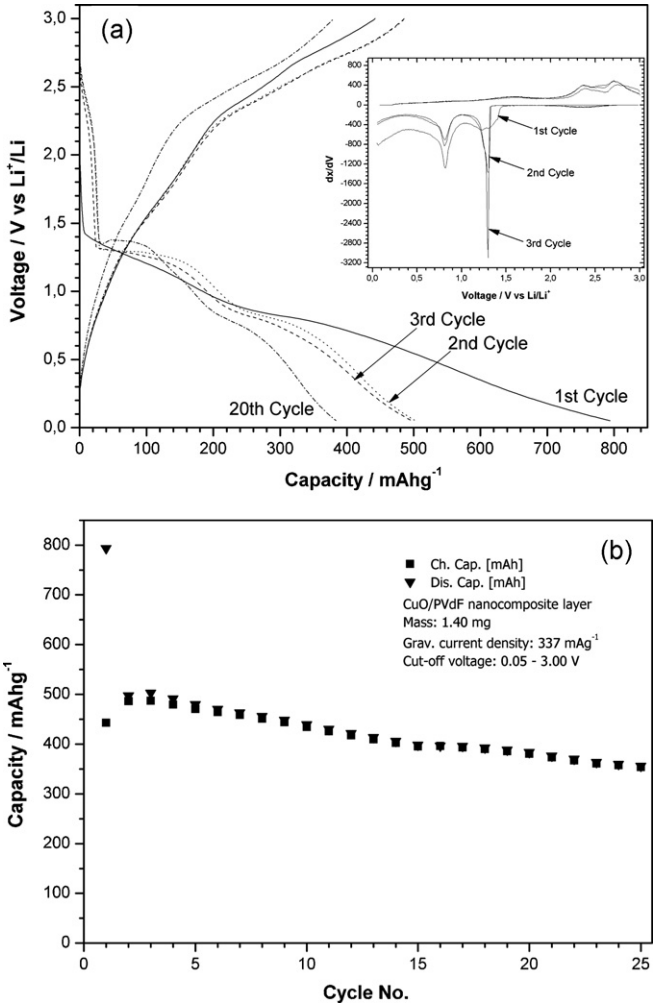

Fig. 8. Galvanostatic measurements of the composite CuO/PVdF electrode between 0.05 and 3.0 V at 337 mAg^{-1}: (a) charge–discharge voltage profiles. The inset is a graph representing the differential capacity. (b) Capacity retention upon progressive charge–discharge.

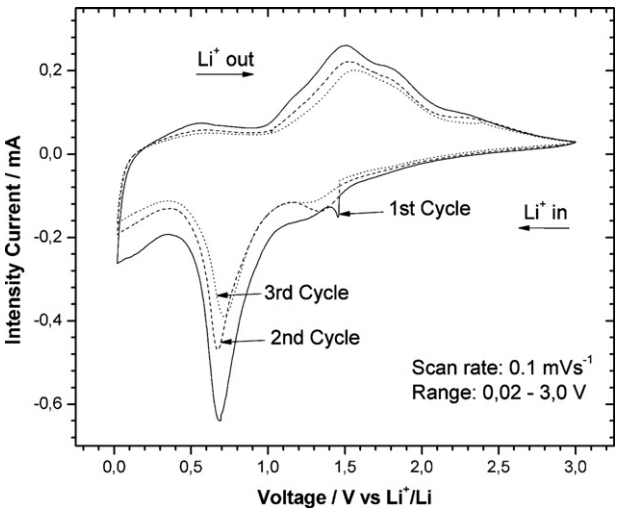

Fig. 9. CV plot for the Fe_2O_3/PVdF electrode deposited by ESP.

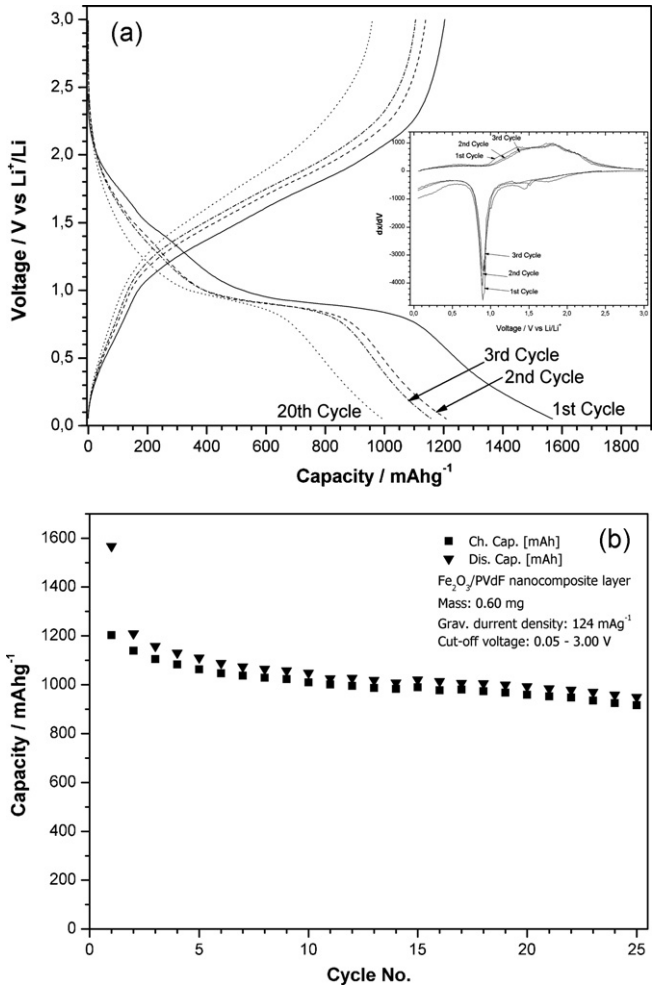

Fig. 10. Galvanostatic measurements of the composite Fe_2O_3/PVdF electrode between 0.05 and 3.0 V at 124 mAg^{-1}: (a) charge–discharge voltage profiles. The inset is a graph representing the differential capacity. (b) Capacity retention upon progressive charge–discharge.

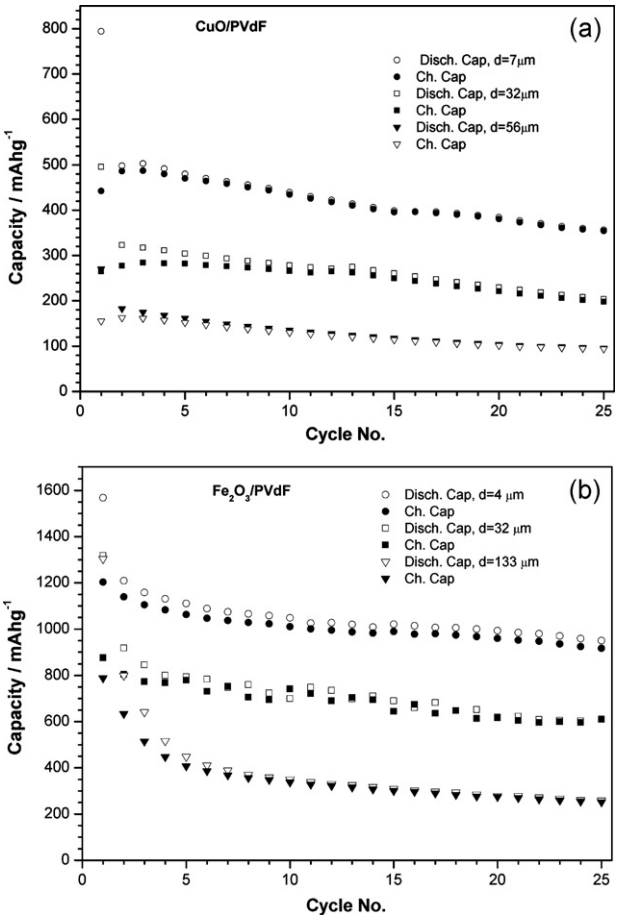

Fig. 11. Capacity retention upon repeated charge–discharge for electrodes with different thickness: (a) CuO/PVdF and (b) Fe_2O_3/PVdF.

The shape of the observed CV is consistent with the plot of the differential capacity, shown in the inset of Fig. 10(a) The discharge–charge curves of the Fe_2O_3/PVdF electrode in Fig. 10(a) indicate that high capacities can be reached. Indeed, an initial discharge capacity of about 1550 mAh g^{-1} is obtained at a gravimetric current density of 124 mAg^{-1}. The discharge profile displays an initial slope with a slight inflection around 1.5 V and a definite plateau around 0.9 V, followed by another slope at lower voltages corresponding to the conversion reaction of the iron oxide. These values are close to the redox peaks found in the CV curves and there is a relation between the major peaks in the CV plot and the definite plateaus in the voltage profiles of discharge–charge.

The evolution of the charge and discharge capacities upon cycling is presented in Fig. 10(b). Despite the irreversible loss in the first cycle and a slight fading of the capacity in the subsequent cycles, the electrode shows a remarkable capacity of about 950 mAh g^{-1} after 25 cycles. It should be mentioned that also in this case the nanocomposite electrode was able to cycle without any conductive additive and despite the poor electrical conductivity of iron oxide and the insulating properties of PVdF.

Finally, the influence of the thickness of the coatings on the capacity retention for the two different types of composite electrodes is presented in Fig. 11.

Not surprisingly, from Fig. 11(a and b) it is observed that for both oxide materials the best performances are obtained in correspondence of thinner electrode coatings. It is important to note that the electrode kinetics in composite electrodes can be divided into three steps [33]: (i) transport of the charge carriers (i.e., Li^+ and e^-) from their source to the surface of the active particles, (ii) charge incorporation, involving the transfer of both charged species from the outside to the inside of the particles and (iii) transport of the Li component inside the particles. Herein CuO and Fe_2O_3 nanoparticles with size below 10 nm and narrow size distribution have been produced and homogeneously inter-dispersed with PVdF, therefore it is reasonable to expect that the characteristic times for steps (ii and iii) are much shorter than that related to step (i), due to the increased surface area of the nanoparticles and their extremely reduced size, respectively [10,11]. In this case, the electrode resistance is proportional to the electrode thickness (or, equivalently, the electrode mass, see Fig. 2), since the thicker the electrode, the longer the average path of the charge carriers for step (i).

The absence of carbon black in both preparations limits the electron percolation between the nanoparticles and, at a certain point, with increasing electrode thickness, a conductive additive is needed to sustain the applied current density without losing capacity. In particular, a previous study [34] comparing bulk, nanoparticulate and mesoporous Fe_2O_3 addresses the various aspects that affect the rate of conversion electrodes, demonstrating that for this type of conversion reaction electron transport to and within the active particles is the limiting factor. Therefore, Fig. 11 and the above considerations suggest that only thin layers in the range of micrometers, containing these nanoparticles, can cycle properly at the examined current densities. Indeed, in order to exploit the positive features of nanoparticles in these composite

electrodes it is convenient either to have thin layers, where percolation is not an issue, or add a conductive additive to the precursors, in order to compensate for the growth of the overall resistance of the electrode as its thickness increases. Finally, in both cases it is also of paramount importance to optimize the ratio of the various components, depending on the specific requirements for their practical application and cycling conditions.

4. Conclusions

Nanostructured composite electrodes based on Fe_2O_3 and CuO were successfully fabricated by electrostatic spray pyrolysis of precursor solutions containing iron and copper salts dissolved in the presence of PVdF. Small oxide nanoparticles were directly synthesized and homogeneously dispersed with the PVdF binder to produce coated electrodes in one step. The small size of the generated Fe_2O_3 and CuO nanoparticles, as well as their homogenous distribution in the composite coatings, enable electrochemical cycling of these electrodes even in the absence of conductive additives. Besides, the even inter-dispersion of the polymer binder on the nanoscale promotes the mutual adhesion of the nanoparticles in the deposits, acting at the same time as a barrier against their growth and agglomeration during both the synthesis process (i.e., inside the reacting droplets) and the electrochemical cycling, thus reinforcing the electrode and the overall contact with the current collector.

Initial discharge capacities are as high as 800 mAh g^{-1} and 1550 mAh g^{-1} for CuO and Fe_2O_3, respectively. The capacity retained after 25 cycles is about 360 mAh g^{-1} for copper oxide and 950 mAh g^{-1} for iron oxide in thin electrodes. These preliminary results indicate that this approach can be used for the direct production of nanocomposite electrode coatings, provided that the thickness of the grown layers does not hinder the electronic conduction in the whole electrode. In this respect, the deposition of thin films with a minimal amount of binder and no conductive additive is highly desirable to conveniently employ the features of the formed nanoparticles and to increase the overall energy density of the electrodes and improve their power delivery. Nevertheless, when thicker electrodes are required, it is likely necessary to include a conductive additive in the preparation, especially in presence of active materials that are poor e^- conductors. In this way, some shortcomings of conversion materials, e.g., initial irreversibility, limited capacity retention and slow reaction kinetics in bulk powders, can be addressed by proper electrode preparation via ESP. Indeed, one can select dedicated precursor solutions/suspensions containing all the needed components and control the composition, morphology, texture and thickness of the deposited composite layers with the active nanoparticles. The large voltage hysteresis between charge and discharge displayed by conversion materials is an intrinsic drawback that has been related to the energy barrier which must be overcome to break the M–X bonds (where X can be: F, O, S, or P). As a matter of fact, this phenomenon is particularly pronounced for fluorides and oxides, while sulfides and phosphides suffer less from it. Therefore, substituting oxygen with phosphine in the proposed synthesis process could be a possible approach to address this main issue. Moreover, the process is simple and can be conveniently optimized. The key ideas underlying this approach, as well as the possibility of synthesizing a wide variety of functional nanocomposite materials by this method will be discussed more in detail in a forthcoming paper.

Acknowledgments

The authors would like to acknowledge the EC for funding the FP7 project E-STARS (ICT-223927), and the Alistore European Research Institute and the Dutch Ministry for Economic Affairs via Agentschap.nl (SenterNovem) for additional financial support.

References

[1] K. Ozawa, Solid State Ionics 69 (1994) 212.
[2] M. Lazzari, B. Scrosati, J. Electrochem. Soc. 127 (1980) 773.
[3] M. Winter, J.O. Besenhard, M.E. Spahr, P. Novak, Adv. Mater. 10 (1998) 725.
[4] P. Poizot, S. Laurelle, S. Grugeon, L. Dupont, J.M. Tarascon, Nature 407 (2000) 496.
[5] J.M. Tarascon, S. Grugeon, M. Morcrette, S. Laruelle, P. Rozier, P. Poizot, C. R. Chim. 8 (2005) 9.
[6] P. Poizot, S. Laurelle, S. Grugeon, L. Dupont, J.M. Tarascon, J. Power Sources 97–98 (2001) 235.
[7] Y. Wu, B. Tan, Y. Li, Nano Lett. 8 (2008) 265.
[8] P. Balaya, H. Li, L. Kienle, J. Maier, Adv. Funct. Mater. 13 (2003) 621.
[9] L. Dupont, S. Laruelle, S. Grugeon, C. Dickinson, W. Zhoub, J.M. Tarascon, J. Power Sources 175 (2008) 502.
[10] P.G. Bruce, B. Scrosati, J.M. Tarascon, Angew. Chem. 47 (2008) 2930.
[11] A.S. Aricò, P. Bruce, B. Scrosati, J.M. Tarascon, W. VanSchalkwijc, Nat. Mater. 4 (2005) 366.
[12] P. Balaya, A.J. Bhattacharyya, J. Jamnik, Y.F. Zhukovskii, E.A. Kotomin, J. Maier, J. Power Sources 159 (2006) 171.
[13] N. Meethong, H.Y.S. Huang, W.C. Carter, Y.M. Chiang, Electrochem. Solid-State Lett. 10 (2007) A134.
[14] J. Maier, Nature 4 (2005) 805.
[15] S.G. Kim, K.H. Choi, J.H. Eun, H.J. Kim, C.S. Hwang, Thin Solid Films 377–378 (2000) 694.
[16] T. Nguyen, E. Djurado, Solid State Ionics 138 (2001) 191.
[17] C.H. Chen, E.M. Kelder, J. Schoonman, J. Power Sources 68 (1997) 377.
[18] A.A. van Zomeren, E.M. Kelder, J.C.M. Marijnissen, J. Schoonman, J. Aerosol. Sci. 25 (1994) 1229.
[19] C.H. Chen, E.M. Kelder, P.J.J.M. van der Put, J. Schoonman, J. Mater. Chem. 6 (1996) 765.
[20] C.H. Chen, E.M. Kelder, J. Schoonman, J. Mater. Sci. 31 (1996) 5437.
[21] Y. Yu, J.L. Shui, C.H. Chen, Solid State Commun. 135 (2005) 485.
[22] H.S. Ryu, J.S. Kim1, Z. Guo, H. Liu, K.W. Kim, J.H. A, H.J. Ahn, Phys. Scripta T139 (2010) 014066 (Fe_2O_3).
[23] M. Mohamedi, S.J. Lee, D. Takahashi, M. Nishizawa, T. Itoh, I. Uchida, Electrochim. Acta 46 (2001) 1161.
[24] D. Munao, J.W.M. van Erven, M. Valvo, E. Garcia-Tamayo, E.M. Kelder, J. Power Sources (2010), doi:10.1016/j.jpowsour.2010.11.072.
[25] J. Hassoun, G. Derrien, S. Panero, B. Scrosati, Adv. Mater. 20 (2008) 3169.
[26] J.H. Lee, B.S. Kong, Y.K. Baek, S.B. Yang, H.T. Jung, Nanotechnology 20 (2009).
[27] A. Debart, L. Dupont, P. Poizot, J.B. Leriche, J.M. Tarascon, J. Electrochem. Soc. 148 (2001) A1266.
[28] F.S. Ke, L. Huang, G.Z. Wei, L.J. Xue, J.T. Li, B. Zhang, S.R. Chen, X.Y. Fan, S.G. Sun, Electrochim. Acta 54 (2009) 5825–5829.
[29] D.W. Zhang, T.H. Yi, C.H. Chen, Nanotechnology 16 (2005) 2338.
[30] H. Liu, G. Wang, J. Park, J. Wang, C. Zhang, Electrochim. Acta 54 (2009) 1733.
[31] H. Liu, G. Wang, J. Wang, D. Wexler, Electrochem. Commun. 10 (2008) 1879–1882.
[32] Y. Piao, H.S. Kim, Y.-E. Sung, T. Hyeon, Chem. Commun. 46 (2010) 118–120.
[33] M. Gaberscek, J. Power Sources 189 (2009) 22–27.
[34] F. Jiao, J. Bao, P.G. Bruce, Electrochem. Solid-State Lett. 10 (2007) A264–A266.